Numerical Heat Transfer, Part A, 48: 359–385, 2005

ISSN: 1040-7782 print/1521-0634 online
DOI: 10.1080/10407780590957134

Taylor & Francis
Taylor & Francis Group

A NUMERICAL STUDY OF FLUID FLOW AND HEAT TRANSFER OVER A BANK OF FLAT TUBES

Haitham M. S. Bahaidarah and N. K. Anand
Department of Mechanical Engineering, Texas A&M University, College Station, Texas, USA

H. C. Chen
Department of Civil Engineering, Texas A&M University, College Station, Texas, USA

The present study considers steady laminar two-dimensional incompressible flow over both in-line and staggered flat tube bundles used in heat exchanger applications. The effects of various independent parameters, such as Reynolds number (Re), Prandtl number (Pr), length ratio (L/Da), and height ratio (H/Da), on the pressure drop and heat transfer were studied. A finite-volume-based FORTRAN code was developed to solve the governing equations. In all, 10 modules were considered in this study. The flow is observed to attain a periodically fully developed condition downstream of the fourth module. The nondimensionalized pressure drop decreases monotonically with an increase in the Reynolds number. In general, the module average Nusselt number increases with an increase in the Reynolds number. The results at Pr = 7.0 indicate a significant increase in the computed module average Nusselt number when compared to those for Pr = 0.7. The overall performance of the in-line configuration for lower height ratio (H/Da = 2) and higher length ratio (L/Da = 6) is preferable since it provides higher heat transfer rate for all Reynolds numbers except for the lowest Re value of 25. As expected, the staggered configurations perform better than the in-line configuration from the heat transfer point of view. Also from the heat transfer point of view, equivalent circular tubes perform better than flat tube banks. However, the heat transfer performance ratio was always greater than 1, signifying that from the pressure-drop point of view the flat tube banks perform better than a tube bank with equivalent circular tubes.

INTRODUCTION

Some studies have shown that the tube shapes and their arrangement in heat exchangers have positive influence on heat transfer [1–3]. Flat tube designs have been recently introduced for use in modern heat exchanger applications such as automotive radiators [4] Flat tubes seem to have favorable pressure drop characteristics compared to circular tubes. Also due to smaller wake size compared to

Received 13 December 2004; accepted 31 January 2005.
Support for this research by King Fahd University of Petroleum and Minerals is gratefully appreciated.
Haitham M. S. Bahaidarah is presently at King Fahd University of Petroleum and Minerals, Dhahran, Saudi Arabia.
Address correspondence to N. K. Anand, Department of Mechanical Engineering, Texas A&M University, College Station, TX 77843-3123, USA. E-mail: nkanand@tamu.edu

NOMENCLATURE

a	coefficients	u, v	Cartesian velocity components, velocity projection
b	source term	V	velocity vector, volume
C_p	specific heat	x, y	Cartesian coordinates
e, w, n, s	adjacent faces to the main point P	Γ	diffusion coefficient
E, W, N, S	adjacent points to the main point P	θ	nondimensional temperature
f	friction factor	μ	dynamic viscosity
F	flow rate through control volume	ν	kinematic viscosity
h	heat transfer coefficient	ρ	mass density
H	height	ξ, η	curvilinear coordinates
J	total flux	ϕ	general dependent variable
Ja	Jacobian of transformation	**Subscripts**	
k	thermal conductivity	av	average
L	length	b	bulk
LMTD	log-mean temperature difference	in	inlet
NP	normalized pressure	max	maximum
Nu	Nusselt number	min	minimum
P	point, pressure, Peclet number	nb	neighboring points
PDF	periodically fully developed flow	NO	nonorthogonal
Q	total heat flux	P	primary flux, main point
Re	Reynolds number	S	secondary flux
S	source term, surface	w	wall
t	time	**Superscripts**	
T	temperature	*	guessed value
		$'$	corrected value

circular tubes, flat tubes have better noise and vibration characteristics. Heat transfer and pressure drop characteristics of flat-tube heat exchangers in the open literature are rather limited. The geometry of flat tubes makes it difficult to study heat transfer and fluid flow using finite-difference and finite-volume techniques. Finite-difference techniques use coordinate transformation and grid-generation techniques to exploit their simplicity and efficiency, as mentioned by Napaolitano and Orlandi [5]. Finite-volume techniques are increasingly used for computing incompressible flow in arbitrary geometries because of recent developments in grid-generation techniques.

The finite-volume method was originally developed as a special case of the finite-difference formulation. Some of the earlier finite-volume approaches were developed for orthogonal coordinate systems because fewer terms result from coordinate transformation. Sharatchandara [6] mentioned that this approach is limited due to the difficulty of maintaining orthogonality throughout the entire domain and the undesirable grid clustering that results from the forced orthogonality constraints. The generalized nonorthogonal coordinate system approach appears to be the most appropriate choice for the majority of the recent finite-volume approaches, not only because of its generality, but also because it is possible to orient the dependent variable along the grid lines conforming to the shape of the domain

and therefore usually along principal streamlines, which minimizes the chance of false diffusion [7].

When Cartesian velocity components are retained as dependent variables and the coordinates are transformed, such formulation of the governing equations is considered partial transformation. This technique has been used extensively in the past, primarily because of its simplicity. Cartesian velocity components have been widely used as the dependent variables in nonorthogonal coordinate systems [8, 9].

A brief review of various studies involving flow over a variety of shapes with various types of flow conditions is worth mentioning at this time. The effect of flow past bluff bodies, especially cylinders, has been a major attraction for fluid mechanics investigations for a long time. Most of these studies concerned flow over a circular cylinder. Williamson [10] and Zdrakovich [11] wrote comprehensive reviews on this topic.

Chang [12] has developed a numerical scheme to predict the heat transfer and pressure drop coefficient in cross flow through rigid tube bundles. The scheme uses the Galerkin finite-element technique. The conservation equations for laminar steady-state flow are cast in function and vorticity form. Chang's numerical predictions agree well with the experimental data up to a Reynolds number value of 1,000.

Kundu [13, 14] studied numerically the heat transfer and fluid flow over a row of in-line cylinders placed between two parallel plates. Incompressible, two-dimensional, and laminar flow were considered. The cylinder and plate temperatures were assumed to be constant but not necessarily the same. The spacing between cylinders altered the flow in the separated zone and subsequently affected the heat transfer. The heat transfer data for various aspect ratios and Reynolds numbers were reduced to form a single formula for ease of interpolation. In general, the pressure drop and heat transfer were spatially periodic, indicating periodically fully developed characteristics.

Grannis and Sparrow [15] studied fluid flow over an array of diamond-shaped fins using a finite-element method. Flow and conjugate heat transfer in a high-performance finned oval tube heat exchanger element were calculated for a thermally and hydrodynamically developing three dimensional laminar flow by Chen [16, 17].

Breuer [18] investigated in detail the confined flow around a cylinder of square cross section mounted inside a plane channel (blockage ratio $B = 1/8$) by two entirely different numerical techniques, a lattice-Boltzmann automata (LBA) method and a finite-volume method (FVM). The finite-volume code was based on an incompressible Navier–Stokes solver for arbitrary nonorthogonal, body fitted grids. Velocity profiles and integral parameters such as drag coefficient, recirculation length, and Strouhal numbers were investigated.

Studies of flat-tube heat exchangers are also limited, though they are expected to have lower air-side pressure drop and better air-side heat transfer coefficients when compared to circular-tube heat exchangers. The pressure drop is expected to be lower than that for circular tubes because of a smaller wake area. For the same reason, vibration and noise are expected to be less in flat-tube heat exchangers compared to circular-tube heat exchangers.

The main objective of this article is to study numerically the 2-D laminar incompressible flow and heat transfer over a flat tube bank (Figure 1). Both in-line and staggered configurations are considered.

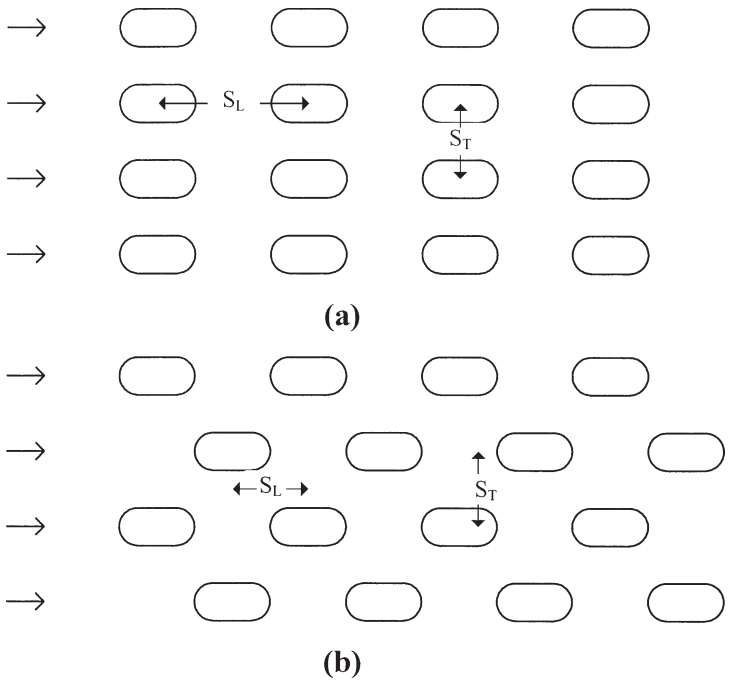

Figure 1. Flat tube banks: (*a*) in-line and (*b*) staggered configurations.

MATHEMATICAL FORMULATION

The equations governing the conservation of mass, momentum, and energy can be cast into general form as

$$\frac{\partial(\rho\phi)}{\partial t} + \nabla \cdot \vec{\boldsymbol{J}} = S \tag{1}$$

where

$$\vec{\boldsymbol{J}} = \rho\vec{\boldsymbol{V}}\phi - \Gamma\nabla\phi \tag{2}$$

In these equations, ϕ is a general dependent variable, ρ is the mass density, Γ is the effective diffusion coefficient, $\boldsymbol{V}$ is the velocity vector, and S designates the volumetric source or sink. In Eq. (2), $\boldsymbol{J}$ corresponds to the total flux of ϕ i.e., it takes into account both convective and diffusive fluxes. Assuming constant thermophysical properties of the fluid, expressions in Cartesian vector notation for steady-state incompressible flow are

$$\text{Continutity:} \qquad \nabla \cdot \boldsymbol{V} = 0 \tag{3}$$

$$\text{Momentum:} \qquad \rho(\boldsymbol{V} \cdot \nabla)\boldsymbol{V} = -\nabla P + \mu\nabla^2\boldsymbol{V} \tag{4}$$

$$\text{Energy:} \qquad \rho C_p(\boldsymbol{V} \cdot \nabla)T = k\nabla^2 T \tag{5}$$

A finite-volume technique proposed by Karki [19] has been used to discretize the general conservation equation. Integration of flux equation leads to

$$(J_{P,e} - J_{S,e}) - (J_{P,w} - J_{S,w}) + (J_{P,n} - J_{S,n}) - (J_{P,s} - J_{S,s}) = S\,\mathrm{Ja} \tag{6}$$

J_p and J_s are referred to the primary flux and secondary flux, respectively. The primary flux a has both convection and diffusion terms, while the secondary flux is solely diffusive and arises as a result of the nonorthogonality of the coordinate system; it would disappear in an orthogonal coordinate system, thus highlighting the fact that the nonorthogonality is one of the many sources of false diffusion. Ja is the Jacobian of transformation.

The secondary fluxes have to be calculated explicitly in order to avoid a nine-point formulation. These terms turn out to be less significant if the grid is almost orthogonal. Terms representing the secondary fluxes will be treated as source terms. The primary flux includes the value of ϕ and its gradient at the control-volume interface. The power-law scheme is used to represent the solution for one-dimensional convection-diffusion equation [20].

Following Patankar's formulation, the primary flux $J_{P,e}$ [Eq. (6)], which combines both convective and diffusive fluxes, is evaluated using a polynomial expression in terms of the cell Peclet number as follows:

$$J_{P,e} = F_e\phi_E + A(|P_e|)D_e(\phi_p - \phi_E) \tag{7}$$

where $A(|P_e|)$ is the polynomial expression defined by Patankar [7]. The non-dimensional cell Peclet number P, is defined as the measure of the relative strengths of the advection through a control surface, F, and the diffusion conductance, D.

Substituting the expression for the primary fluxes and the source term, the discretization equations that constitue a set of linear algebraic equations which were solved to get the value of ϕ at nodal points in the computation domain can be written as

$$a_p\phi_p = a_E\phi_E + a_w\phi_w + a_N\phi_N + a_S\phi_S + b \tag{8}$$

where

$$a_E = D_eA(|P_e|) + \max[\![0, -F_e]\!] \tag{9}$$

$$a_w = D_WA(|P_w|) + \max[\![0, F_w]\!] \tag{10}$$

$$a_N = D_nA(|P_n|) + \max[\![0, -F_n]\!] \tag{11}$$

$$a_s = D_sA(|P_s|) + \max[\![0, F_s]\!] \tag{12}$$

$$a_P = a_E + a_W + a_N + a_S - S_P\,\mathrm{Ja} \tag{13}$$

The source b in Eq. (8) can be expressed as $b = b_s + b_{\mathrm{NO}}$, where $b_s = S_C\,\mathrm{Ja}$ and b_{NO} is the source term due to the nonorthogonality of the coordinate system.

If the curvilinear velocities are chosen as the dependent variables in the momentum equations, then they will have curvature source terms, as these

curvilinear velocity do not have a fixed direction. Karki [19] presented a formulation in which the curvature source terms are obtained by algebraic manipulation of the discretization equations. This would eliminate the complications and difficulties of programming these extra terms if the discretization equations were obtained by the conventional methods. These curvature source terms could be avoided if the discretization is carried out in a locally fixed coordinate system. In Karki's formulation, the derived discretization equation includes parallel velocities, instead of the actual velocities, at the neighboring points for the velocity (e.g., $u_{\xi,P}$) in a local coordinate system, as shown in Figure 2.

For highly nonorthogonal grids, the numerical scheme of the discretization equation as such may not give a converged solution. This problem can be eliminated by adding and subtracting the actual velocities in the discretization equation as follows:

$$\begin{aligned} a_P u_{\xi,P} = {} & a_E u_{\xi,E} + a_W u_{\xi,W} + a_N u_{\xi,N} + a_S u_{\xi,S} + b \\ & + a_E\left(\bar{u}_{\xi,E} - u_{\xi,E}\right) + a_W\left(\bar{u}_{\xi,W} - u_{\xi,W}\right) \\ & + a_N\left(\bar{u}_{\xi,N} - u_{\xi,N}\right) + a_S\left(\bar{u}_{\xi,S} - u_{\xi,S}\right) \end{aligned} \tag{14}$$

The same procedure can be used to find the discretized equation in the η direction to be solved along with the above equation for the velocity field. The solution of the pressure field can be found by coupling the momentum equation with the continuity equation using the Semi-Implicit Method for Pressure–Linked Equations (SIMPLE) algorithm of Patankar and Spalding [20]. Following this technique, the resulting pressure-correction equation can be cast into the following form:

$$a_P P'_P = a_E P'_E + a_w P'_W + a_N P'_N + a_S P'_S + b + b_{\mathrm{NO}} \tag{15}$$

where

$$a_E = \alpha_{\xi,e}\rho_e \frac{\Delta V}{a_e\,\Delta x} \tag{16}$$

$$a_W = \alpha_{\xi,w}\rho_w \frac{\Delta V}{a_w\,\Delta x} \tag{17}$$

$$a_N = \alpha_{\eta,n}\rho_n \frac{\Delta V}{a_n\,\Delta y} \tag{18}$$

$$a_S = \alpha_{\eta,s}\rho_s \frac{\Delta V}{a_s\,\Delta y} \tag{19}$$

$$a_P = a_E + a_W + a_N + a_S \tag{20}$$

and

$$b = \left(\alpha_\xi \rho u^*_\xi\right)_w - \left(\alpha_\xi \rho u^*_\xi\right)_e + \left(\alpha_\eta \rho u^*_\eta\right)_s - \left(\alpha_\eta \rho u^*_\eta\right)_n \tag{21}$$

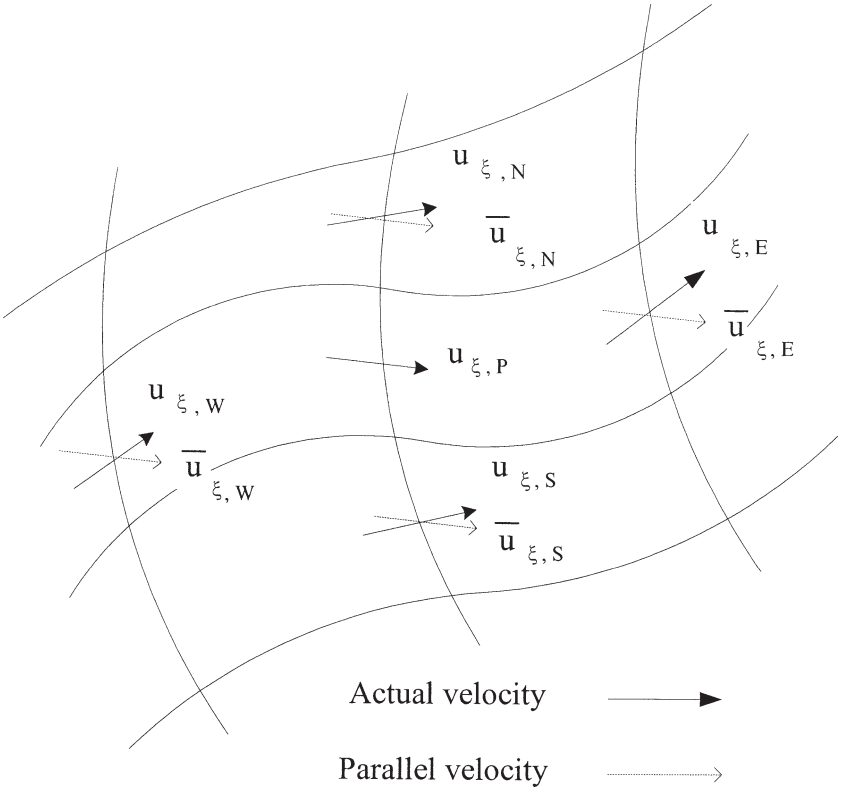

Figure 2. Actual and parallel neighboring velocity to $u_{\xi,P}$.

$$b_{\mathrm{NO}} = (\beta_\xi \rho u_\eta)_e - (\beta_\xi \rho u_\eta)_w + (\beta_\eta \rho u_\xi)_n - (\beta_\eta \rho u_\xi)_s \tag{22}$$

where superscript (*) and ($'$) denote the guessed and corrected fields, respectively. The momentum equations and the pressure-correction equation are solved iteratively until convergence is achieved.

INDEPENDENT PARAMETERS

The in-line and staggered geometric configurations considered are shown in Figure 1. The configuration is characterized by transverse pitch S_T and longitudinal pitch S_L measured between the tube centers. Figure 3 shows an enlarged view of two rows of an in-line flat tube bank that illustrates the domain of interest. The rows in the flow geometry are assumed to be of infinite extent in the direction perpendicular to the paper, so that the flow pattern can be considered as two-dimensional. Therefore, the computational domain is limited to the one shown in Figure 3 by the hatched lines. The longitudinal tube diameter Db is twice the length of a circular cylinder with diameter Da. The height H is

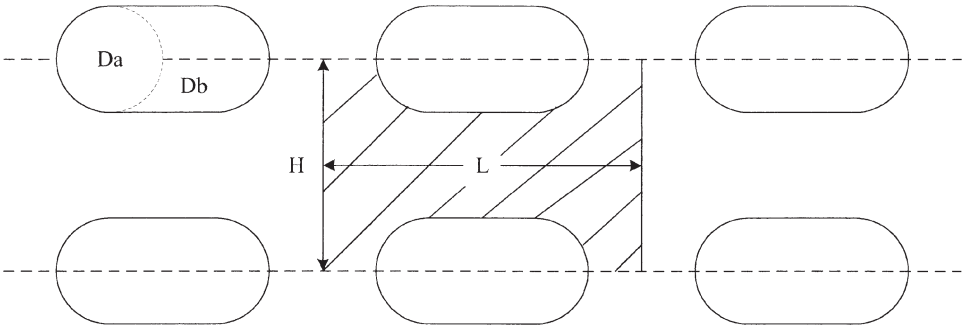

Figure 3. Enlarged view of two rows of an in-line flat tube bank.

equivalent to the transverse distance between two rows or the height of one module, and L is the longitudinal distance between the tube centers of two successive cylinders or the length of one module.

In this work, four different geometric configuration are considered. These configurations are shown in Figure 4 for a single module. All these configurations are considered with different values of H/Da and L/Da Calculations were made for five different Re values ($\mathrm{Re} = 25$, 50, 100, 200, and 400) and for two different Prandtl numbers ($\mathrm{Pr} = 0.7$). In all, 180 cases were studied. However, only representative cases are chosen for discussion in this article. Re is defined as

$$\mathrm{Re} = \frac{u_b D_H}{\nu} \tag{23}$$

where D_H is taken to be twice the height H.

The value L/Da for the module of an in-line configuration is taken to be 4, as shown in Figure 4*a*. The other three configuration are all staggered in position, and the L/Da values are 7, 6, and 5, as shown in Figures 4*b*, 4*c*, and 4*d*, respectively. Although half of the domain of an in-line module can be studied because of symmetry, the entire domain is studied to make sure that the results are symmetric, which in itself is a degree validation.

GRID AND BOUNDARY CONDITIONS

In each configuration, the domain needs to be discretized into a structured grid by using one of the grid-generation techniques. The Geometry and Mesh Building Intelligent Toolkit (GAMBIT) was used for this task to handle the arbitrary-shaped domain by which a body-fitted coordinate system was generated, and the irregular physical domain was discretized into numerous square volumes. The resulting grid distribution for a single in-line module is illustrated in Figure 5.

The computational domain was divided into three individual regions. These regions are the entry region, the flats tube modules, and the exit region. A uniform orthogonal grid was used for both entry and exit regions. The grid distribution

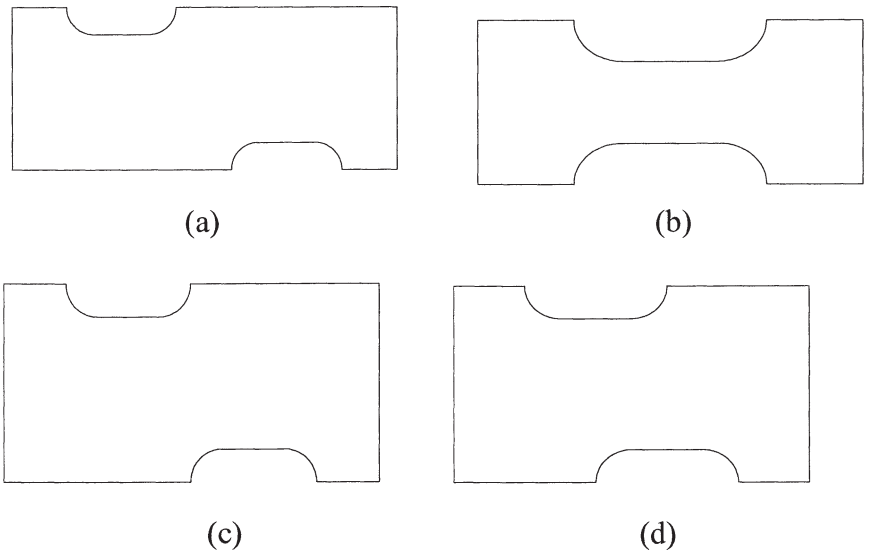

Figure 4. Configurations for a single module of: (*a*) in-line, L^*4; (*b*) staggered, L^*7; (*c*) staggered, L^*6; (*d*) staggered, L^*5.

shown above (Figure 5) can be repeated successively to generate the domain of flat tube modules. In this study, 10 consecutive flat tubes were included in the computational domain.

In Figure 5, the surfaces *BC* and *FG* are the top wall of the bottom tube and the bottom wall of the top tube, respectively. A no-slip boundary condition was assigned for these two surfaces, where both velocity components were set to zero at that boundary ($u = v = 0$). These surfaces were subjected to constant wall temperature ($T = T_w$) condition. The lines *AB*, *CD*, *EF*, and *GH* are lines of symmetry where no flow crosses these boundaries and the normal component of velocities and the normal gradient of the parallel component of velocity are set to zero. Finally, the lines *AH* and *DE* are recognized as the module inlet and module outlet, respectively. A uniform inlet velocity profile was assigned at the inlet boundary condition ($u = U_{\text{in}}$). A constant inlet temperature ($T = T_{\text{in}}$), different than the wall temperature, was assigned at the channel inlet. The streamwise gradients of all variables were set to zero at the outlet boundary.

CONVERGENCE CRITERIA

The discretization equations obtained by integrating the governing partial differential equations resulted in a set of linear algebraic equations for each variable which need to be solved iteratively. Within each iteration, the set of linear algebraic equations were solved sequentially. A set of these equations was solved using a line-by-line method which is a combination of the tri-diagonal matrix algorithm and the Gauss-Siedel procedure. Convergence could be declared if the maximum of the absolute value of the mass residues was less than a very small number ε

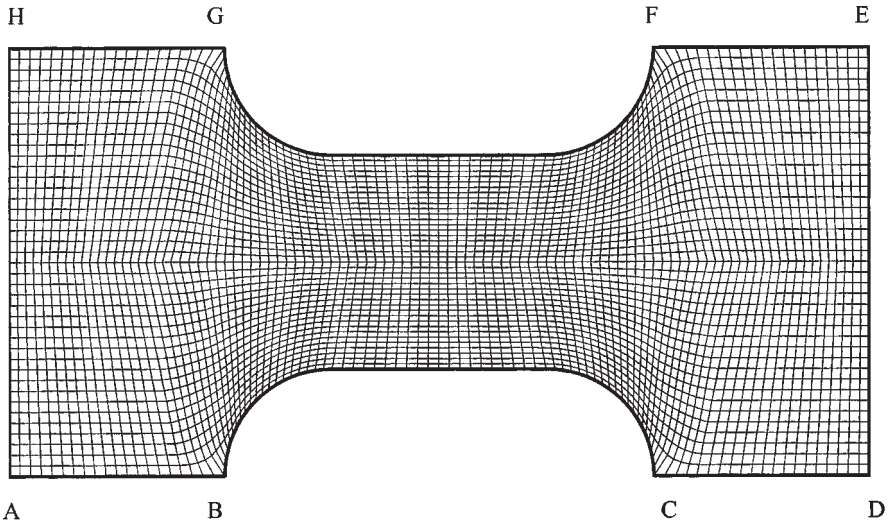

Figure 5. Grid distributions for a single in-line configuration module.

(e.g., 10^{-5}). In this study, convergence was declared by monitoring the sum of the residues at each node. Since the magnitude of u_ξ and u_η are not known *a priori*, monitoring the relative residuals is more meaningful. The relative convergence criteria for u_ξ and u_η and are defined as follows:

$$\bar{R}_{u_\xi} = \frac{\sum_{\text{nodes}} \left| a_e u_{\xi,e} - \sum a_{\text{nb}} u_{\xi,\text{nb}} - b_{u_{\text{NO}}} - A_e (P_P - P_E) \right|}{\sum\limits_{\text{nodes}} \left| a_e u_{\xi,e} \right|} \leq \varepsilon_{u_\xi} \tag{24}$$

$$\bar{R}_{u_\eta} = \frac{\sum_{\text{nodes}} \left| a_n u_{\eta,n} - \sum a_{\text{nb}} u_{\eta,\text{nb}} - b_{u_{\text{NO}}} - A_n (P_P - P_N) \right|}{\sum\limits_{\text{nodes}} \left| a_n u_{\eta,n} \right|} \leq \varepsilon_{u_\eta} \tag{25}$$

In the pressure equation, it is appropriate to check for mass imbalance in the continuity equation.
The convergence criterion for pressure was defined as follows:

$$R_P = \sum\nolimits_{\text{nodes}} |b + b_{\text{NO}}| \leq \varepsilon_P \tag{26}$$

The convergence criteria for temperature were defined as

$$R_T = \sum\nolimits_{\text{nodes}} \left| a_P T_P - \sum a_{\text{nb}} T_{\text{nb}} - b_{T\cdot\text{NO}} \right| \leq \varepsilon_T \tag{27}$$

The numerical iteration criterion required that the normalized residuals of mass, momentum, and energy be less than 10^{-6} for all cases considered in this study.

VALIDATION

The code developed here was validated by reproducing solutions for some benchmark problems. The fluid flow and heat transfer in a parallel-plate channel subjected to constant wall temperature were predicted. The Nusselt number for the fully developed region between two parallel plates subjected to constant wall temperature using the developed code is 7.56, which agrees favorably with the Nusselt number value of 7.54 mentioned by many authors, such as Incropera and DeWitt [21].

Fluid flow and heat transfer over a row of in-line cylinders placed between two parallel plates was studied numerically by Kundu et al. [13]. They computed the flow field using a finite-difference method. The physical domain was transformed into a computational domain so that a rectangular domain could be used. The fluid was assumed to be incompressible, with constant thermophysical properties. The numerical results were obtained by solving the vorticity and the stream-function equations in dimensionless form. The entire domain was divided into several heat exchanger modules (HEMs). Each HEM contained one cylinder and was bound by two fictitious surfaces located at the midsection between two consecutive cylinders. Except for the first and the last HEM, the pressure drop and Nusselt number across a HEM were almost constant for any specified Re.

Nondimensionalized pressure drop computed using the developed code is compared with the numerical predictions of Kundu et a1. [13] and experimental data of Kundu [22] in Figure 6. It is evident that there is a very good agreement between the results obtained by the developed code and results in the literature [12, 22], thus further validating the code. The average heat transfer coefficient and the corresponding Nusselt number across the HEMs were also computed and studied. The computed enthalpy between the HEMs was integrated to calculate the normalized bulk temperature $\theta_{b,i}$ at the inlet and exit of each HEM. The heat flow Q_i for each HEM was computed by calculating the local heat flux and integrating the results over all the surfaces of the HEM. The average heat transfer coefficient $\bar{h}$ was introduced so that

$$Q_i = \dot{m} c_P (\theta_{b,i} - \theta_{b,i-1}) = \bar{h}(1 - \theta_{m,i})(2A_P + A_i) \tag{28}$$

where the subscript i represents the module number, A is the area of the circular cylinder, A_P is the area of the plate, and $\theta_{m,i}$ is the average of the normalized bulk temperatures at the inlet and exit of each HEM, defined as

$$\theta_{m,i} = 0.5(\theta_{b,i} + \theta_{b,i-1}) \tag{29}$$

Table 1 shows the average the Nusselt number (Nu) at two different Reynolds numbers. The average Nusselt number is defined as $\mathrm{Nu} = \bar{h} D_H / k$, and the hydraulic diameter D_H is defined as the channel height (H). The geometric parameter values

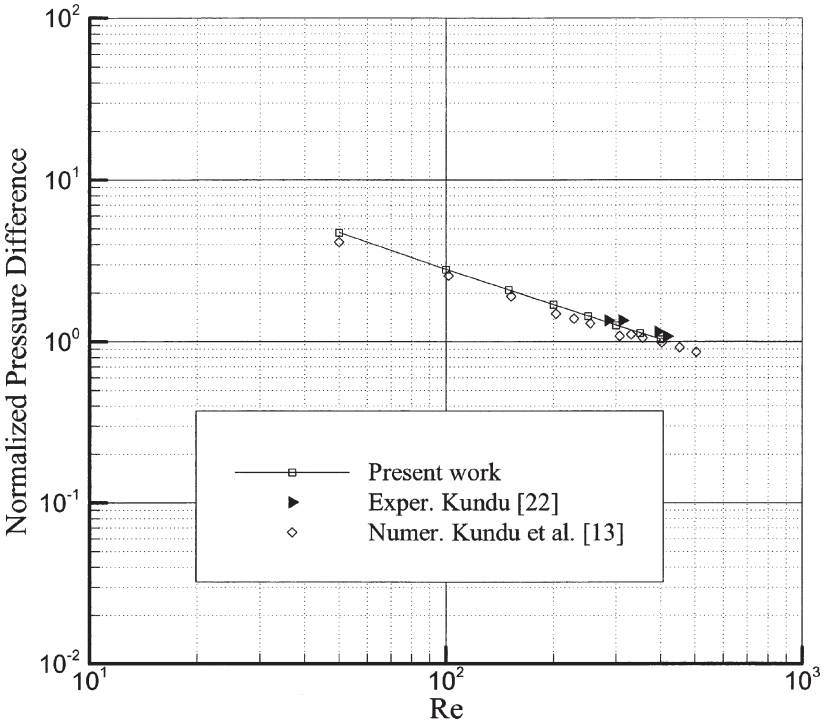

Figure 6. Normalized pressure difference across the third HEM.

were $L/D = 3$ and $H/D = 2$ for the cases considered for validation. It is evident from Table 1 that the numerical predictions of heat transfer using the developed code agree very well with the numerical predictions of Kundu [13].

GRID INDEPENDENCE

The following parameters were considered in the grid independence test; $\mathrm{Db/Da} = 2$, $H/\mathrm{Da} = 4$, $L/\mathrm{Da} = 4$, and $\mathrm{Pr} = 0.7$ at the highest Reynolds number of 400 for the in-line configuration. The grid independence test was done for

Table 1. Average Nusselt number for $L/D = 3$ and $H/D = 2$

	2nd HEM	3rd HEM	4th HEM
Re = 50			
Kundu et al. [13]	9.4	9.4	9.8
Present work	9.228	9.229	9.229
Re = 200			
Kundu et al. [13]	12.5	12.6	12.8
Present work	12.44	12.43	12.42

several grid sizes per module. These grids were 101×101, 101×121, 126×121, 126×151, and 151×151 per module for 10 modules, in addition to the uniform grid points in the entry and exit regions. It is evident from Tables 2 and 3 that the maximum percentage difference in friction factor and average Nusselt number for any module obtained by two successive grid sizes is less than 1%. Accordingly, to minimize error and to optimize CPU resources, all parametric runs were made with 101×101 grid.

RESULTS AND DISCUSSION

The governing independent parameters influencing the fluid flow and heat transfer over a bank of flat tubes are the Reynolds number (Re), Prandtl number (Pr), height ratio (H/Da), length ratio (L/Da), the aspect ratio of the tube (Db/Da), and the configuration or the positioning of the tubes (i.e., in-line or staggered). Table 4 shows all of the configurations considered in this study. Each case is assigned a different name and studied for a different combination of the Reynolds numbers ($\mathrm{Re} = 25$, 50, 100, 200, and 400) and two different Prandtl numbers representing air and water ($\mathrm{Pr} = 0.7$ and 7.0).

Although 180 different parametric runs were made, only representative results are presented in this work, more detail can be found in Bahaidarah [23]. The effect of each parameter on the velocity profile, streamline, normalized temperature field, normalized pressure drop, and module average Nusselt number will be discussed.

Figure 7 shows the streamwise developing velocity profiles along the exit of each module. The velocity distribution is normalized by the value of the uniform inlet velocity (Uo) and given as a function of Y/H, for both in-line and staggered configurations. It can be established that as the Reynolds number increases, the maximum velocity in the passage increases, whereas the negative velocity downstream, right behind the tubes, increases in magnitude to satisfy continuity. The velocity profile is nearly symmetric and repeats itself for other modules, except the first and the last, due to entrance and exit effects. The flow is not fully developed in the first module. Its profile is similar to other modules at low values of Reynolds number. At the exit of the last module, the velocity profile is slightly different due to the absence of additional tubes downstream.

Comparison of Figure 7*a* with Figures 7*c* and 7*e* shows the most noticeable changes in velocity profiles. These changes are due to the increase in the height ratio. The maximum velocity in the middle (Y/H) of the passage decreases considerably because of a larger flow area. The negative velocity in magnitude, downstream right behind the tube, increases as the height ratio decreases. The flow attains periodicity in further upstream modules as the height ratio decreases. For instance, when $\mathrm{Re} = 400$ at $H/\mathrm{Da} = 2$, the flow attains a periodicity downstream of the second module, as illustrated in Figure 7*a*. However, at the same Re for $H/\mathrm{Da} = 3$ or 4, the flow attains a periodicity downstream of the fourth module, as illustrated in Figures 7*c* and 7*e*.

The maximum velocity decreases slightly as the length ratio increases. The velocity profile flattens as the length ratio increases. This is because the flow has

Table 2. Grid independence test—friction factor

Module	Grid 1 (101 × 101)	Grid 2 (101 × 121)	Percentage difference	Grid 3 (126 × 121)	Percentage difference	Grid 4 (126 × 151)	Percentage difference	Grid 5 (151 × 151)	Percentage difference
1	0.727	0.725	0.203	0.727	0.167	0.729	0.367	0.728	0.109
2	0.233	0.232	0.468	0.234	0.960	0.235	0.198	0.236	0.503
3	0.202	0.201	0.389	0.203	0.840	0.203	0.062	0.204	0.463
4	0.180	0.179	0.368	0.180	0.780	0.180	0.024	0.181	0.487
5	0.167	0.166	0.386	0.167	0.752	0.167	0.021	0.168	0.498
6	0.159	0.158	0.424	0.159	0.746	0.159	0.043	0.160	0.446
7	0.154	0.153	0.441	0.154	0.723	0.154	0.076	0.155	0.321
8	0.151	0.150	0.419	0.151	0.667	0.151	0.104	0.152	0.175
9	0.149	0.148	0.381	0.149	0.602	0.149	0.115	0.150	0.085
10	0.137	0.136	0.465	0.137	0.740	0.137	0.186	0.138	0.128

Table 3. Grid independence test—average Nusselt number

Module	Grid 1 (101 × 101)	Grid 2 (101 × 121)	Percentage difference	Grid 3 (126 × 121)	Percentage difference	Grid 4 (126 × 151)	Percentage difference	Grid 5 (151 × 151)	Percentage difference
1	27.925	27.866	0.213	27.793	0.261	27.717	0.273	27.682	0.129
2	16.141	16.120	0.130	16.098	0.136	16.064	0.213	16.062	0.012
3	14.499	14.483	0.110	14.446	0.258	14.415	0.217	14.402	0.090
4	13.670	13.657	0.096	13.619	0.282	13.593	0.191	13.576	0.121
5	13.270	13.256	0.105	13.221	0.265	13.197	0.184	13.179	0.138
6	13.074	13.059	0.115	13.027	0.239	13.001	0.201	12.985	0.127
7	12.978	12.962	0.121	12.931	0.236	12.906	0.200	12.890	0.125
8	12.932	12.917	0.118	12.886	0.240	12.860	0.200	12.843	0.131
9	12.910	12.896	0.110	12.864	0.250	12.838	0.201	12.821	0.134
10	12.720	12.706	0.109	12.688	0.148	12.662	0.202	12.652	0.075

Percentage difference $= |[\text{Grid(I)} - \text{Grid(I} + 1)]/\text{Grid(I} + 1)|^{*}100$

Table 4. In-line and staggered configurations considered in this study

Configuration	H/DA	L/DA	Configuration	H/Da	L/Da
In-line, H^*2–L^*4	2	4	Stagg., H^*2–L^*5	2	5
In-line, H^*2–L^*5	2	5	Stagg., H^*2–L^*6	2	6
In-line, H^*2–L^*6	2	6	Stagg., H^*2–L^*7	2	7
In-line, H^*3–L^*4	3	4	Stagg., H^*3–L^*5	3	5
In-line, H^*3–L^*5	3	5	Stagg., H^*3–L^*6	3	6
In-line, H^*3–L^*6	3	6	Stagg., H^*3–L^*7	3	7
In-line, H^*4–L^*4	4	4	Stagg., H^*4–L^*5	4	5
In-line, H^*4–L^*5	4	5	Stagg., H^*4–L^*6	4	6
In-line, H^*4–L^*6	4	6	Stagg., H^*4–L^*7	4	7

enough length to recover to the condition of uniform inlet velocity profile before being interrupted by the presence of the next tube module. This behavior is not shown because it illustrates a less significant effect. However, the changes in length due to different spacing between the upper and lower tubes in staggered arrangements are shown in Figures 7*b*, 7*d*, and 7*f*. The symmetric condition is no longer applicable as this arrangement comes into consideration.

The changes in results are more noticeable for the inner four modules with the first and the last, especially at higher values of Reynolds numbers ($\mathrm{Re} = 200$ and 400). It has to be noted that the location of maximum velocity has been shifted slightly to the top due to the absence of an obstacle (i.e., flat tube) at the top. As the longitudinal spacing (S_L) between the upper and lower tubes decreases, the velocity tends to have higher values at the location of the maximum velocities as well as negative velocity due to small tube spacing.

As can be seen from the velocity profiles presented earlier, most of the cases attain periodically fully developed condition downstream of the first module (the fourth in some cases). Thus, discussion of the fourth module will be enough to show most of the details needed for examining the streamlines, instead of showing the entire domain with dense repeated information. Figures 8*a*, 8*c,* and 8*e* show the effect of Reynolds number on the nondimensional stream function for the fourth module for an in-line arrangement, for $H/\mathrm{Da} = 2$ and $L/\mathrm{Da} = 4$. Flow separation can hardly be detected when Reynolds number as low as 25. As Reynolds number increase, the separated flow covers a smaller portion of the domain until it completely covers the area between two consecutive tubes at higher Reynolds number. In fact, the entire area between two consecutive tubes is occupied by recirculation at $\mathrm{Re} = 200$ and 400, though the center of the recirculation is shifted slightly to the right, closer to the next tube, at $\mathrm{Re} = 400$. This significant difference is a result of a higher flow speed, which pushes the recirculation downstream a bit.

The streamlines shown in Figures 8*a*, 8*c*, and 8*e* are symmetric, but their magnitudes are not, as the stream functions are set to 0 and 1 at $Y/H = 0$ and 1, respectively. For the staggered arrangement the streamlines are no longer symmetric between two adjacent rows of flat tubes. Figures 8*b*, 8*d*, and 8*f* show the effect of different values of tube spacing between the upper and lower rows (i.e., $H/\mathrm{Da} = 2$

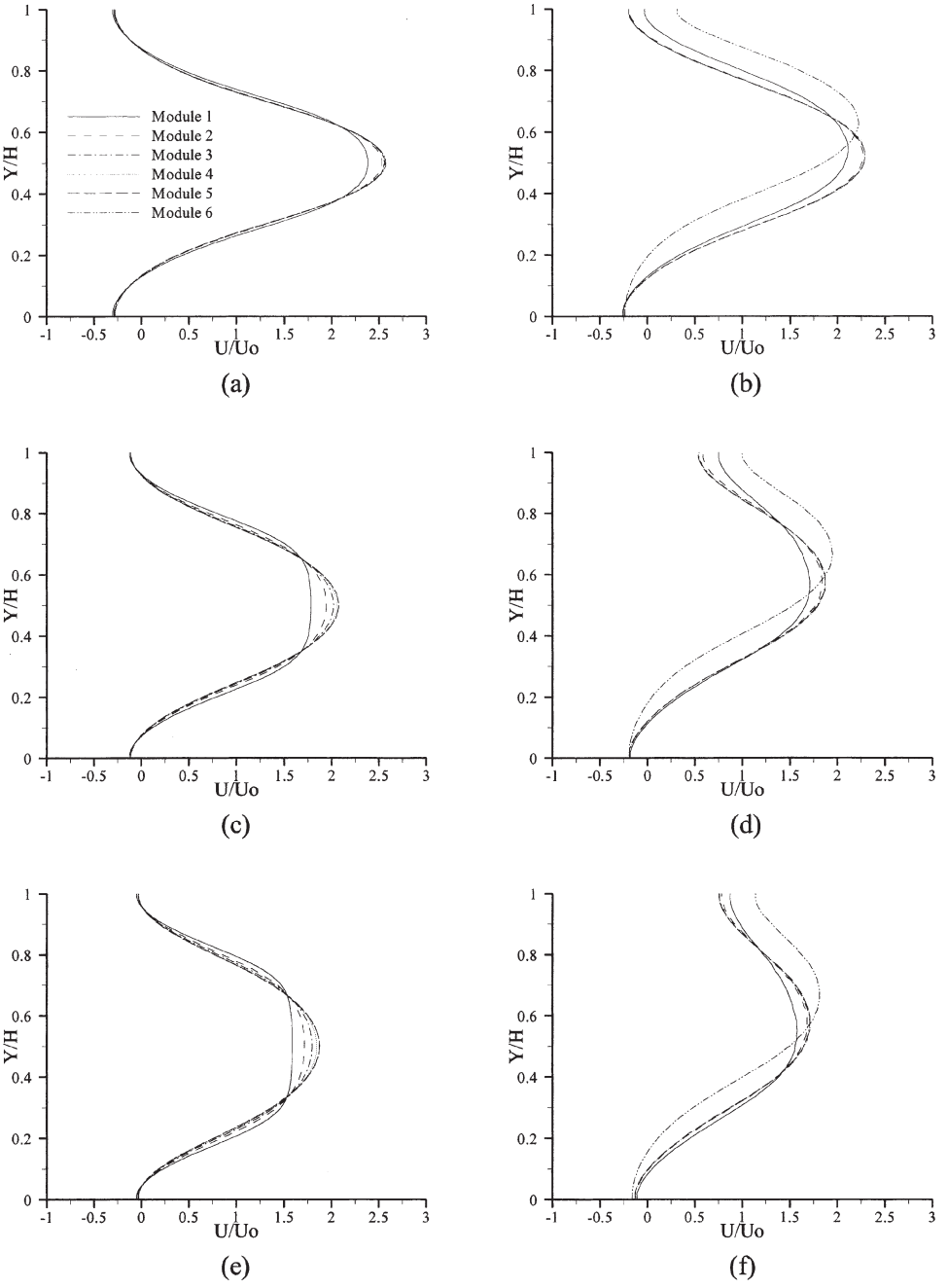

Figure 7. Developing velocity profiles at each module outlet (MO) for both in-line and staggered arrangements at Re = 400: (*a*) in-line, H^*2–L^*4; (*b*) staggered, H^*2–L^*5; (*c*) in-line, H^*3–L^*4; (*d*) staggered, H^*2–L^*6; (*e*) in-line, H^*4–L^*4; (*f*) staggered, H^*2–L^*7.

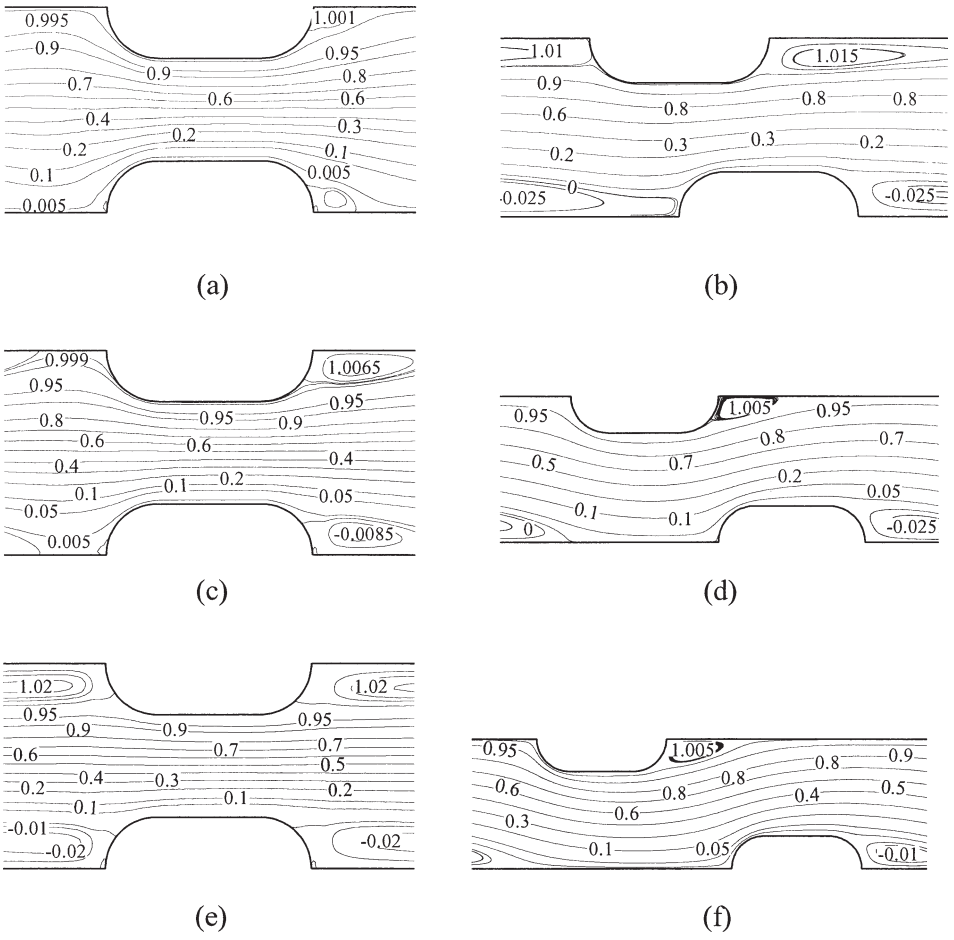

Figure 8. Nondimensional stream function for the fourth module for both in-line and staggered arrangements: (*a*) in-line, H^*2–L^*4, Re = 50; (*b*) staggered, H^*2–L^*5, Re = 400; (*c*) in-line, H^*2–L^*4, Re = 200; (*d*) staggered, H^*2–L^*6, Re = 400; (*e*) in-line, H^*2–L^*4, Re = 400; (*f*) staggered, H^*2–L^*7, Re = 400.

and $L/\mathrm{Da} = 5$, 6, and 7) on the nondimensional stream function for the fourth module at Re = 400. The recirculation behind the upper tube is smaller in size when compared to the one behind the lower tube. This is due to the fact that half of the lower tube is located vertically in the same position as the recirculation behind the upper tube, which pushes the streamlines toward the top. This restricts the upper recirculation and results in minimizing its size due to the reduction in the flow cross-sectional area.

The spacing between the upper and lower tubes can be increased by shifting the lower tube toward the right. When all the lower tubes push the streamlines to the top, the recirculation behind the upper tubes becomes smaller and even disappear at moderate Reynolds number (Re = 100). Further increase in the spacing between the upper and lower tubes does not decrease the upper recirculation. In fact, the

Table 5. Minimum and maximum values of stream function (ψ^*), for both in-line and staggered configurations, $H/\mathrm{Da} = 2$, $\mathrm{Re} = 400$

	In-line arrangement		Staggered arrangement	
L/Da	$\Psi^*_{\min}$	$\Psi^*_{\max}$	$\Psi^*_{\min}$	$\Psi^*_{\max}$
4	–0.0265	1.0224	—	—
5	–0.0263	1.0225	–0.0514	1.0191
6	–0.0268	1.0228	–0.0275	1.0067
7	—	—	–0.0176	1.0077

recirculation increases because there is enough distance between the rear edge of the upper tube and the front edge of the lower tube for the flow to expand as shown in Figure 8*f*. This fact is documented in Table 5, which lists the minimum and maximum values of nondimensional stream function at $\mathrm{Re} = 400$.

Figures 9*a* and 9*b* show the effect of Reynolds number on the normalized temperature lines (isotherms). All isotherms range from 0 to 1, which represents a low fluid temperature at the inlet to higher fluid temperature as it reaches the hot tube surface. As the Reynolds number increases, the lower value isotherms penetrate deeper, which means the colder fluid is getting closer to the hot surface. As a result of this behavior, the heat transfer is increased, as will be shown later in the computed Nusselt number. A comparison of Figures 9*c* and 9*d* with Figure 9*a* shows the effect of varying the height and length ratios on the isotherms. An increase in height ratio makes the cold isotherms penetrate farther downstream. However, the colder isotherms are farther from the hot tube surface, which implies lower heat transfer. The impact of varying length ratio on isotherms is minimal and thus does not have much of an impact on heat transfer. For in-line arrangement of flat tubes, the symmetric condition is preserved because of symmetric geometry. This is not the case for the staggered arrangement with different length spacing, as shown in Figure 9*e*. It is clear that the flow is pushed up as a result of the presence of the lower tube. All isotherms given above, Figures 9*a*–9*e*, are for air ($\mathrm{Pr} = 0.7$). Figure 9*f* has the same parameters as Figure 9*a* except for the Prandtl number. Increase in Pr significantly affects distribution of isotherms. At a higher value of Pr the isotherms are more densely packed, implying better heat transfer. This behavior is more pronounced at higher Reynolds numbers ($\mathrm{Re} = 400$).

Since the velocity profile is nearly symmetric (for the in-line arrangement only) and repeats itself for other modules, the pressure drop across the modules has spatially periodic behavior. This is the primary reason that the computed pressure drop is nearly constant for all modules except the first and the last. Numerical data for dimensionless pressure differences across the interior modules for both in-line and staggered arrangements can be found in Table 6. The data show that the values are nearly constant for a given Reynolds number and a fixed set of aspect ratios.

Figure 10 provides the normalized pressure drop for the fourth module for both in-line and staggered configurations. Figure 10*a* shows the impact of height ratio on the normalized pressure drop at fixed length ratio ($L/\mathrm{Da} = 4$). As the height

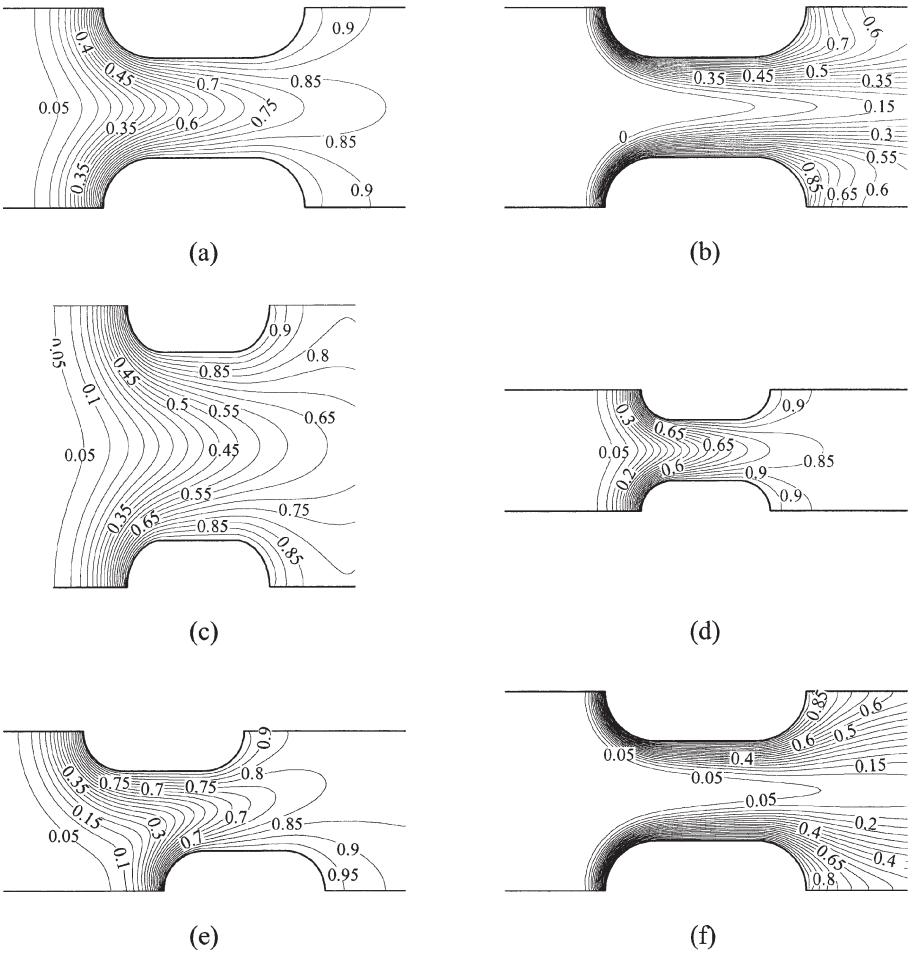

Figure 9. Isotherms for the fourth module for both in-line and staggered arrangements: (*a*) in-line, H^* 2–L^*4, Re = 25; (*b*) in-line, H^*2–L^*4, Re = 200; (*c*) in-line, H^*3–L^*4, Re = 25; (*d*) in-line, H^*2–L^*6, Re = 25; (*e*) staggered, H^*2–L^*5, Re = 25; (*f*) in-line, H^*2–L^*4, Re = 25, Pr = 7.0.

ratio increases, the normalized pressure drop decreases. Figure 10*b* shows the impact of length ratio on the normalized pressure drop at fixed height ratio ($H/\mathrm{Da} = 2$). It can be clearly stated that the length ratio has very little effect or even a negligible effect on pressure drop. As expected, the normalized pressure drop decreases monotonically with an increase in Re. The normalized pressure drop behavior for a staggered configuration, is similar to that for an in-line configuration, as shown in Figures 10*c* and 10*d*.

Tables 7 and 8 show the computed average Nusselt number for the interior modules for both in-line and staggered arrangements at Pr = 0.7 and 7.0, respectively. As expected, the average Nusselt number is higher for Pr = 7.0 compared to that for Pr = 0.7. From these tables, it is evident that for a given Reynolds number the module average Nusselt number remains fairly constant, thus signifying the existence of a

Table 6. Modules ΔP^* for both in-line and staggered arrangements at selected Reynolds numbers

		In-line arrangement				Staggered arrangement			
H/DA	Re	2nd	3rd	4th	5th	2nd	3rd	4th	5th
		$L/\mathrm{Da} = 4$				$L/\mathrm{Da} = 5$			
2	25	9.094	9.102	9.114	9.125	7.845	7.844	7.840	7.836
	100	2.665	2.652	2.649	2.647	2.490	2.484	2.484	2.483
	400	1.049	0.968	0.970	0.941	1.115	0.943	0.925	0.921
3	25	3.336	3.338	3.339	3.339	3.568	3.563	3.562	3.561
	100	0.942	0.914	0.912	0.912	1.079	1.052	1.055	1.055
	400	0.375	0.314	0.284	0.269	0.465	0.363	0.341	0.330
4	25	2.055	2.059	2.060	2.060	2.379	2.371	2.372	2.372
	100	0.584	0.549	0.543	0.542	0.690	0.662	0.661	0.661
	400	0.233	0.202	0.180	0.167	0.285	0.233	0.212	0.200
		$L/\mathrm{Da} = 5$				$L/\mathrm{Da} = 6$			
2	25	9.201	9.199	9.191	9.181	4.702	4.696	4.686	4.676
	100	2.823	2.817	2.816	2.817	1.628	1.627	1.627	1.628
	400	1.083	0.975	0.958	1.002	0.746	0.673	0.655	0.652
3	25	3.449	3.448	3.443	3.436	3.025	3.023	3.023	3.022
	100	1.014	0.996	0.996	0.997	0.993	0.976	0.976	0.976
	400	0.423	0.352	0.324	0.320	0.465	0.367	0.344	0.335
4	25	2.165	2.166	2.168	2.170	2.305	2.295	2.295	2.295
	100	0.633	0.604	0.602	0.602	0.710	0.685	0.685	0.685
	400	0.250	0.216	0.198	0.192	0.312	0.245	0.225	0.215
		$L/\mathrm{Da} = 6$				$L/\mathrm{Da} = 7$			
2	25	9.212	9.212	9.210	9.207	3.278	3.276	3.276	3.277
	100	2.928	2.924	2.923	2.922	1.258	1.256	1. 254	1.254
	400	1.154	1.028	1.032	1.046	0.579	0.524	0.511	0.508
3	25	3.490	3.489	3.486	3.482	2.412	2.412	2.415	2.420
	100	1.061	1.049	1.050	1.05!	0.861	0.851	0.852	0.853
	400	0.408	0.310	0.286	0.300	0.416	0.346	0.322	0.314
4	25	2.217	2.221	2.226	2.231	2.026	2.018	2.017	2.017
	100	0.665	0.643	0.642	0.643	0.671	0.650	0.650	0.649
	400	0.273	0.232	0.216	0.215	0.310	0.244	0.224	0.213

thermally periodically fully developed flow condition. However, both in-line and staggered configurations do not attain thermally periodically fully developed condition at $\mathrm{Re} = 400$ for $\mathrm{Pr} = 7.0$. Figures 11*a*–11*d* show the module average Nusselt number for both in-line and staggered arrangements. The qualitative behavior of module average Nusselt number for $\mathrm{Pr} = 7.0$ is similar to that for $\mathrm{Pr} = 0.7$.

The effectiveness of using flat tubes was evaluated by studying the ratio of the module average Nusselt number for periodically fully developed flow of flat tube configurations and the module average Nusselt number for periodically fully developed flow for circular tube configurations. Henceforth, this ratio will be referred to as the heat transfer enhancement ratio ($\mathrm{Nu}_i^+ = \mathrm{Nu}_{i,\mathrm{Flat}}/\mathrm{Nu}_{i,\mathrm{Circular}}$). It

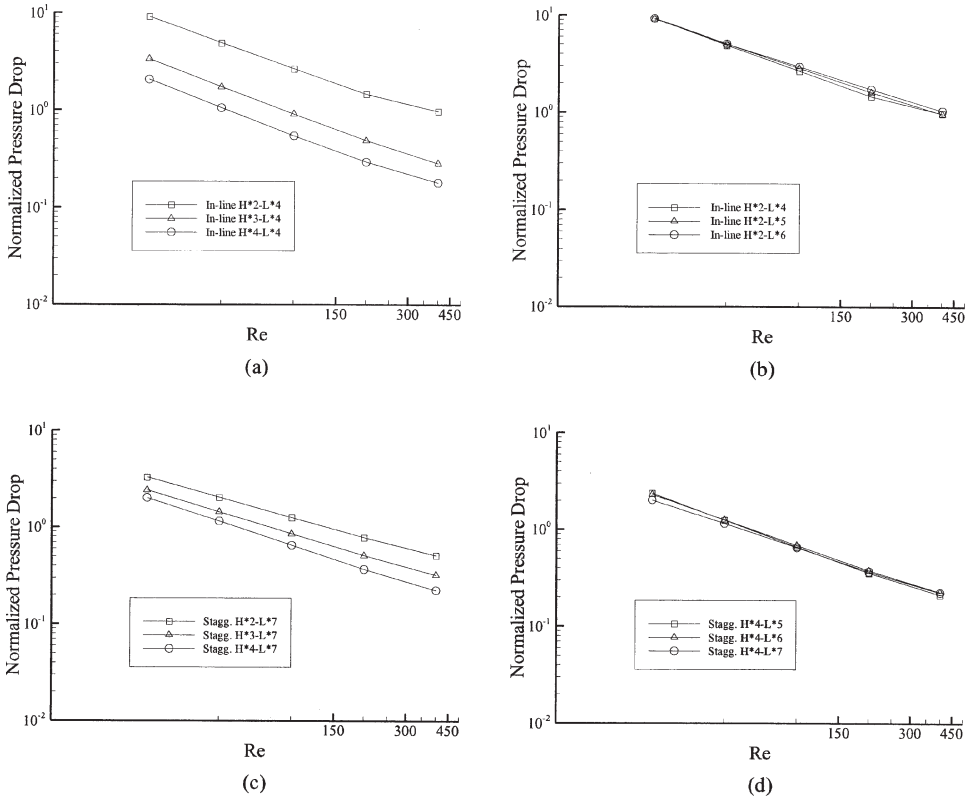

Figure 10. Normalized pressure drop across the fourth module for in-line arrangements: (*a*) in-line, L^*4; (*b*) in-line, H^*2; (*c*) in-line, L^*5; (*d*) in-line, H^*3.

has to be noted that the circumference of a flat tube is equal to that of a circular tube in order to establish a valid comparison.

Table 9 shows the heat transfer enhancement ratio of the fourth module for both in-line and staggered configurations with fixed height ratio ($H/\mathrm{Da} = 3$) and length ratio ($L/\mathrm{Da} = 5$ and 6). The heat transfer enhancement ratio is less than unity, indicating that circular tubes outperform flat tubes. The heat transfer enhancement ratio decreases with an increase in Reynolds number, signifying that the increase in Nusselt number is higher for circular tubes when compared to flat tubes. As expected, the staggered configurations perform better than the in-line configurations from a heat transfer point of view.

The effectiveness of using flat tubes can also be studied by evaluating the heat transfer performance ratio. The heat transfer performance ratio is defined as the ratio of heat transfer enhancement to unit increase in pumping power, which can be written as $\mathrm{Nu}_i^* = \mathrm{Nu}_i^+ / (f_{i,\mathrm{Flat}}/f_{i,\mathrm{Circular}})^{1/3}$. The friction factors are raised to the one-third power, as the pumping power is proportional to the one-third power of the friction factor. For applications where the pumping ratio is of concern, the heat transfer performance ratio should be greater than unity. As evident from Table 10,

Table 7. Average Nusselt number for interior modules for both in-line and staggered arrangements, $Pr = 0.7$

		In-line arrangement				Staggered arrangement			
H/Da	Re	2nd	3rd	4th	5th	2nd	3rd	4th	5th
		$L/Da = 4$				$L/Da = 5$			
2	25	10.38	10.38	10.39	10.39	9.99	9.99	9.99	9.99
	100	14.61	14.60	14.60	14.60	14.63	14.63	14.63	14.63
	400	18.07	17.33	17.29	17.44	19.75	18.78	18.73	18.71
3	25	10.75	10.75	10.75	10.75	10.94	10.94	10.94	10.94
	100	12.86	12.82	12.82	12.82	13.79	13.74	13.75	13.76
	400	16.14	14.74	14.21	14.02	17.45	16.30	15.95	15.86
4	25	10.85	10.85	10.85	10.85	11.52	11.51	11.51	11.51
	100	12.42	12.24	12.23	12.23	13.63	13.50	13.50	13.50
	400	16.14	14.50	13.67	13.27	17.74	16.05	15.35	15.07
		$L/Da = 5$				$L/Da = 6$			
2	25	10.43	10.44	10.44	10.43	8.77	8.78	8.78	8.78
	100	15.16	15.16	15.16	15.15	13.37	13.40	13.40	13.41
	400	19.41	18.73	18.59	18.54	18.09	17.54	17.49	17.49
3	25	11.05	11.05	11.05	11.05	10.46	10.46	10.46	10.46
	100	13.75	13.73	13.73	13.74	13.97	13.95	13.96	13.97
	400	17.24	15.97	15.62	15.52	18.35	17.10	16.82	16.77
4	25	11.46	11.46	11.47	11.47	11.54	11.53	11.54	11.54
	100	13.49	13.38	13.38	13.38	14.31	14.21	14.22	14.23
	400	17.55	15.82	15.12	14.80	18.88	17.16	16.57	16.35
		$L/Da = 6$				$L/Da = 7$			
2	25	10.44	10.45	10.44	10.44	7.80	7.80	7.81	7.81
	100	15.51	15.51	15.51	15.51	12.59	12.64	12.65	12.65
	400	20.07	19.59	19.49	19.45	17.48	17.03	16.98	16.98
3	25	11.15	11.15	11.15	11.15	9.79	9.80	9.80	9.80
	100	14.36	14.35	14.35	14.35	13.80	13.84	13.87	13.87
	400	18.21	17.03	16.74	16.61	18.73	17.55	17.29	17.25
4	25	11.72	11.72	11.73	11.73	11.25	11.25	11.26	11.26
	100	14.26	14.19	14.19	14.19	14.58	14.54	14.57	14.57
	400	18.60	16.93	16.31	16.08	19.69	17.96	17.43	17.25

this ratio is always higher than 1, signifying the importance of such an application from the pumping power point of view.

SUMMARY

A detailed numerical study was conducted on a two-dimensional flow and heat transfer over flat tube bundles found in heat exchanger applications. Both in-line and staggered arrangements were considered in the study. The effects of the Reynolds number (Re), Prandtl number (Pr), length ratio (L/Da), and height ratio (H/Da) on the developing velocity profiles, streamlines, isotherms, pressure drops, and module average Nusselt numbers (Nu) were examined.

Table 8. Average Nusselt number for interior modules for both in-line and staggered arrangements, $Pr = 7.0$

		In-line arrangement				Staggered arrangement			
H/Da	Re	2nd	3rd	4th	5th	2nd	3rd	4th	5th
		$L/Da = 4$				$L/Da = 5$			
2	25	15.70	15.46	15.44	15.44	15.97	15.83	15.82	15.82
	100	21.06	19.16	18.37	17.99	22.05	20.64	20.17	20.00
	400	43.46	37.33	34.88	34.44	52.19	41.95	39.98	39.28
3	25	14.19	13.48	13.31	13.27	15.32	14.71	14.59	14.56
	100	19.37	17.27	16.21	15.57	21.49	19.35	18.37	17.83
	400	35.20	31.17	28.46	26.82	36.91	34.43	32.17	31.11
4	25	14.14	13.11	12.74	12.61	15.59	14.59	14.29	14.19
	100	19.87	17.44	16.21	15.43	22.08	19.57	18.33	17.57
	400	32.67	29.89	27.26	25.59	36.33	32.85	30.27	28.87
		$L/Da = 5$				$L/Da = 6$			
2	25	16.57	16.41	16.40	16.40	14.54	14.48	14.49	14.49
	100	22.00	20.37	19.69	19.39	21.01	19.80	19.36	19.20
	400	46.16	39.72	35.94	33.01	40.92	36.81	35.37	34.78
3	25	15.25	14.66	14.54	14.52	15.48	15.02	14.95	14.94
	100	20.84	18.74	17.69	17.07	22.40	20.31	19.37	18.85
	400	36.07	31.58	29.48	28.14	39.06	35.19	33.11	32.12
4	25	15.35	14.41	14.12	14.03	16.36	15.46	15.22	15.16
	100	21.54	19.09	17.83	17.05	23.57	21.01	19.77	19.00
	400	36.37	31.83	29.41	27.68	38.66	34.63	32.15	30.79
		$L/Da = 6$				$L/Da = 7$			
2	25	17.17	17.06	17.06	17.06	13.53	13.52	13.54	13.55
	100	23.01	21.45	20.83	20.57	20.26	19.24	18.85	18.70
	400	48.11	40.32	36.72	33.62	38.92	35.19	33.71	33.09
3	25	16.00	15.53	15.45	15.43	15.16	14.84	14.81	14.81
	100	22.04	19.99	18.96	18.37	22.51	20.66	19.79	19.31
	400	38.33	33.56	31.43	29.23	40.35	35.64	33.50	32.40
4	25	16.23	15.42	15.19	15.13	16.54	15.82	15.65	15.61
	100	22.90	20.48	19.23	18.46	24.29	21.85	20.65	19.92
	400	38.31	33.24	30.52	28.83	40.76	35.81	33.28	31.81

Numerical data for the dimensionless pressure difference for the interior modules show that the values are nearly constant for a given Reynolds number and a fixed set of geometric ratios, implying that the flow has attained periodicity in interior modules. The module average Nusselt number for $Pr = 0.7$ for a given Re and geometric ratios reaches thermally fully developed flow condition downstream of the second module except for $Re = 400$. In all cases, nondimensionalized pressure drop decreases monotonically with an increase in Reynolds number. On the other hand, the module average Nusselt number increases with an increase in the Reynolds number. The results at $Pr = 7.0$ indicate an increase in the computed module average

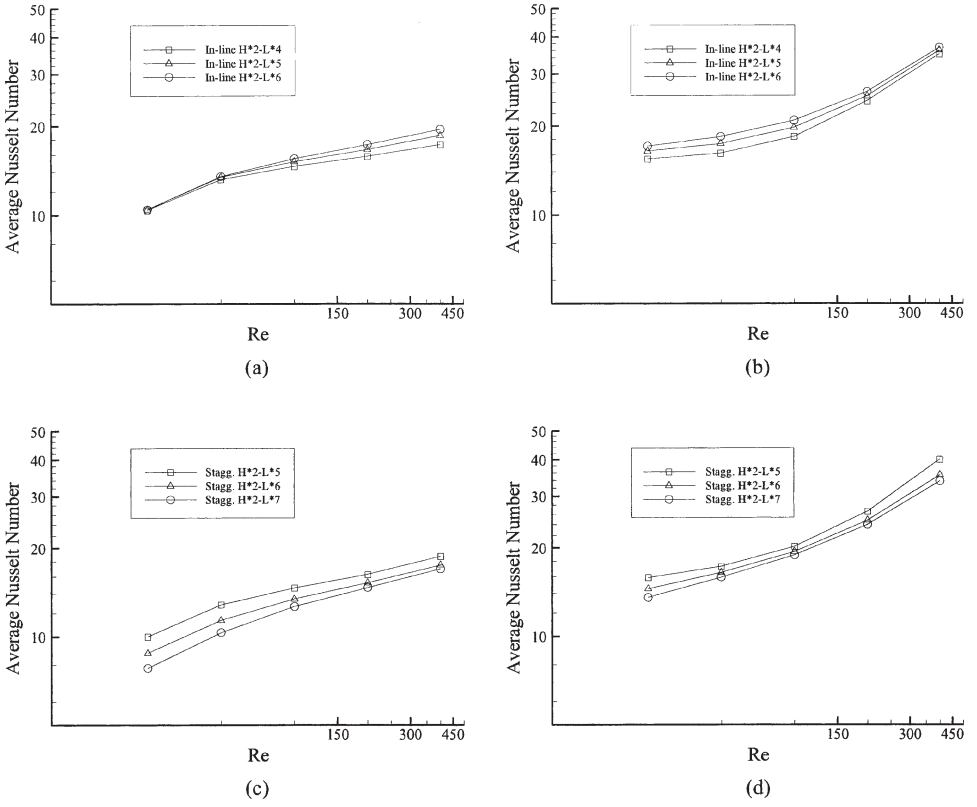

Figure 11. Average Nusselt number for the fourth module, for both in-line and staggered arrangements: (*a*) in-line, H^*2, Pr = 0.7; (*b*) in-line, H^*2, Pr = 7.0; (*c*) staggered, H^*2, Pr = 0.7; (*d*) staggered, H^*2, Pr = 7.0.

Table 9. Heat transfer enhancement ratio (Nu^+) for the fourth module

Re	In-line, H^*3–L^*5	In-line, H^*3–L^*6	Staggared, H^*3–L^*5	Staggared, H^*3–L^*6
25	0.942	0.937	0.944	0.972
50	0.932	0.929	0.931	0.955
100	0.918	0.922	0.918	0.939
200	0.881	0.896	0.886	0.912
400	0.833	0.830	0.785	0.891

Table 10. Heat transfer performance ratio (Nu^*) for the fourth module

Re	In-line, H^*3–L^*5	In-line, H^*3–L^*5	Staggered H^*3–L^*5	Staggered H^*3–L^*6
25	1.154	1.143	1.105	1.056
50	1.165	1.154	1.116	1.070
100	1.175	1.180	1.140	1.096
200	1.152	1.172	1.144	1.125
400	1.067	1.131	1.065	1.323

Nusselt number when compared to that for $Pr = 0.7$. For both in-line and staggered configuration, the flow does not attain a periodically fully developed condition at $Pr = 7.0$ and $Re = 400$.

The heat transfer enhancement ratio is less than unity, which indicates that circular tubes outperform flat tubes from a heat transfer point of view. However, the heat transfer performance ratio is always higher than 1, signifying the importance of such application from the pumping power point of view. As expected, the staggered configurations perform better than the in-line configurations from a heat transfer point of view.

REFERENCES

1. T. Ota, H. Nishiyama, and Y. Taoka, Heat Transfer and Flow around an Elliptic Cylinder, *Int. J. Heat Mass Transfer*, vol. 27, no. 10, pp. 1771–1779, 1984.
2. T. Ota, H. Nishiyama, J. Kominami, and K. Sato, Heat Transfer from Two Elliptic Cylinder in Tandem Arrangement, *J. Heat Transfer*, vol. 108, pp. 525–531, 1986.
3. T. Wung, J. Niethammer, and C. Chen, Measurements of Heat-Mass Transfer and Pressure Drop for Some Non-standard Arrays of Tubes in Cross Flow, in C. Tien, V. Carey, and J. Ferrell (eds.), *Heat Transfer 1986, Proc. Eighth Int. Heat Transfer Conf.*, pp. 1041–1046, Hemisphere, San Francisco, 1986.
4. R. L. Webb, *Principles of Enhanced Heat Transfer*, Wiley, New York, 1993.
5. M. Napolitano and P. Orlandi, Laminar Flow in Complex Geometry: A Comparison, *Int. J. Numer. Meth. Fluids*, vol. 5, pp. 667–683, 1985.
6. M. C. Sharatchandra, A Strongly Conservative Finite Volume Formulation for Fluid Flows in Complex Geometries Using Contra Variant Velocity Components, Ph.D. thesis Texas A&M University, College Station, TX, 1995.
7. S. V. Patankar, *Numerical Heat Transfer and Fluid Flow*, McGraw-Hill, New York, 1980.
8. C. R. Maliska and G. D. Raithby, A Method for Computing Three-Dimensional Flows Using Non-orthogonal Boundary-Fitted Coordinates, *Int. J. Numer. Meth. Fluids*, vol. 4, pp. 519–537, 1984.
9. W. Shyy, S. S. Tong, and S. M. Correa, Numerical Recirculating Flow Calculation Using a Body-Fitted Coordinate System, *Numer. Heat Transfer A*, vol. 8, pp. 99–113, 1985.
10. C. H. K. Williamson, Vortex Dynamics in the Cylinder Wake, *Annu. Rev. Fluid Mech.*, vol. 28, pp. 477–539, 1996.
11. M. M. Zdrakovich, *Flow around Circular Cylinders*, 1: *Fundamentals*, Oxford University Press, New York, 1997.
12. Y. Chang, A. N. Beris, and E. E. Michaelides, A Numerical Study of Heat and Momentum Transfer for Tube Bundles in Cross-Flow, *Int. J. Numer. Meth. Fluids*, vol. 9, pp. 1381–1394, 1989.
13. D. Kundu, A. Haji-Sheikh, and D. Y. S. Lou, Heat Transfer Predictions in Cross Flow over Cylinders between Two Parallel Plates, *Numer. Heat Transfer A*, vol. 19, pp. 361–377, 1991.
14. D. Kundu, A. Haji-Sheikh, and D. Y. S. Lou, Pressure and Heat Transfer in Cross Flow over Cylinders between Two Parallel plates, *Numer. Heat Transfer A*, vol. 19, pp. 345–360, 1991.
15. V. B. Grannis and E. M. Sparrow, Numerical Simulation of Fluid Flow through an Array of Diamond-Shaped Pin Fins, *Numer. Heat Transfer A*, 19, 381–403, 1991.
16. Y. Chen, M. Fiebig, and N. K. Mitra, Conjugate Heat Transfer of a Finned Oval Tube Part A: Flow Patterns, *Numer. Heat Transfer A*, vol. 33, pp. 371–385, 1998.

17. Y. Chen, M. Fiebig, and N. K. Mitra, Conjugate Heat Transfer of a Finned Oval Tube Part A: Flow Patterns, *Numer. Heat Transfer A*, vol. 33, pp. 387–401, 1998.
18. M. Breuer, J. Bernsdorf, T. Zeiser, and F. Durst, Accurate Computations of the Laminar Flow past Cylinder Based on Two Different Methods: Lattice–Boltzmann and Finite-Volume, *Int. J. Heat Fluid Flow*, vol. 21, pp. 186–196, 2000.
19. K. Karki, A Calculation Procedure for Viscous Flows at All Speed in Complex Geometries, Ph.D. thesis, University of Minnesota, Minneapolis, MN.
20. S. V. Patankar and D. B. Spalding, A Calculation Procedure for Heat, Mass and Momentum Transfer in Three-Dimensional Parabolic Flow, *Int. J. Heat Mass Transfer*, vol. 15, 1787.
21. F. P. Incropera and D. P. DeWitt, *Fundamentals of Heat and Mass Transfer*, Wiley, New York, 1996.
22. D. Kundu, Computational and Experimental Studies of Flow Field an Heat Transfer from a Row of In-line Cylinders Centered between Two Parallel Plates, Ph.D. thesis, University of Texas at Arlington, Arlington, TX, 1989.
23. H. M. Bahaidarah, A Numerical Study of Heat and Momentum Transfer over a Bank of Flat Tubes, Ph.D thesis, Texas A&M University, College Station, TX, 2004.